Numerical Study of a Pulsed Auto-Igniting Jet Flame with Detailed Tabulated Chemistry

Eray Inanc[a,*], Andreas M. Kempf[a,b]

[a] *Chair of Fluid Dynamics, Institute for Combustion and Gasdynamics (IVG), University of Duisburg-Essen, Germany*
[b] *Center for Nano-Integration Duisburg-Essen (CENIDE), University of Duisburg-Essen, Germany*

Abstract

This work investigates an auto-igniting impulsively started jet flame issuing into hot and vitiated co-flow by Large-Eddy Simulation (LES) with multidimensional detailed tabulated chemistry. The experiment from DLR (German Aerospace Center, Stuttgart) is reproduced. The combustion model includes the scalar dissipation rate effects and pressure dependency, where the pressure is used to couple the tabulated chemistry to the compressible solver. We identify the effect of (weak) pressure perturbations and analyze auto-ignition (AI) properties in pulsed flames and their variations on different realizations. For the former task, two separate simulations are performed in density- and pressure-based formulations with the same boundary conditions. A good agreement was achieved between both of the solvers and the experiments for the statistically steady jet, providing evidence that the combustion model is suitable for the pulsed jet. Both solvers managed to describe the mixing dynamics well. However, they slightly underpredicted the lift-off height of the flame, where we suspect a minor overestimation of the flame propagation speeds.

The transient jet was simulated for 20 pulse cycles to achieve pulse statistics of AI. The estimated delay times and the location of the AI matched experimental observations. The AI kernels always emerged on the lean-side of the mixing layer at the so-called most-reactive mixture fraction, and at various heights above the burner for each pulse cycle. It was observed that AI was extremely sensitive to the local temperature field, where a slight temperature variation caused a significant change in AI delay time and location. Finally, the statistics showed slight variations between the pulses for the most-reactive mixture fraction, likely caused by turbulent fluctuations of the flow field. Overall, the results show that the tabulated chemistry model is able to reproduce the AI delay time and location with a satisfactory agreement.

Keywords: Pulsed Jets, Auto-ignition, Compressibility Effects, Large-Eddy Simulation (LES), Flamelet

Generated Manifolds (FGM).

1. Introduction

In pulsed fuel jets, transient mixing and auto-ignition (AI) play a significant role in many combustion systems including Diesel engines and direct injection systems, where the control of the combustion is totally governed by AI dynamics. Even small perturbations of temperature, pressure, turbulence intensity, gas composition and scalar dissipation rate influence AI and combustion [1]. The AI dynamics at various temperatures and pressures for different fuels in laminar and turbulent conditions have been investigated experimentally in shock tubes [2] and rapid compression engines [3] as well as in combustion bombs and flames [4], and numerically by direct numerical simulation (DNS) [5] and large eddy simulation (LES) [6] with realistic chemistry modeling. A detailed overview of studies on AI is given in the review paper by Mastorakos [1].

Experimentalists successfully determined the AI delay time and observed the flame kernel and the subsequent development of the flame by advanced high-speed imaging techniques [7, 8, 9, 10, 11]. However, the short time and length scales involved in AI limit the experimental investigations to simple setups. It was observed that AI takes place in the form of local ignition kernels emerging at the most-reactive mixture fraction, away from stoichiometry, at low scalar dissipation rates (SDR) [12].

A DNS would be ideal to study AI dynamics but is still too expensive for large-scale problems. An alternative is LES with detailed chemistry [13, 6]. This approach is attractive for (statistically) steady problems, but still costly for transient cases with a large number of cycles in pulsating jets [14]. As a result, chemistry tabulation methods come to mind in exchange for lesser accuracy.

It is known that an advanced tabulation technique is required for accurate predictions of AI. One candidate is based on Flamelet Generated Manifolds (FGM) [15], which have been extensively validated to model ignition, slow chemistry, flame lift-off, and quenching [16]. Recent developments of the PFGM concept have been reviewed by van Oijen et al. [17]. However, the coupling of FGM to density-based solvers is problematic [18], as the reaction source term is highly sensitive to the pressure perturbations. A simple approach is to analytically extrapolate low-Mach number formulations to the perturbed states [19].

In the present work, the behavior of the AI in pulsating jets is investigated using highly resolved LES in low-Mach and compressible formulations with multi-dimensional FGM. The objectives are to; i. analyze the influence of the compressibility effects during the pulses; ii. determine the AI delay time and the location of the ignition kernel and compare them to the experimental pulse-statistics.

*Corresponding author
Email address: eray.inanc@uni-due.de (Eray Inanc)

Table 1: Thermochemical state of the fuel and the co-flow [11].

Jet		Co-flow				
Z_{st}	T_f [K]	T_o [K]	X_{N_2}	X_{O_2}	X_{H_2O}	X_{OH}
0.0297	290	1490	0.712	0.102	0.178	0.82E-6

2. Experiment

The auto-igniting jet flame Experiment performed by Papageorge et al. [7, 8, 9, 10, 11] conducted at the German Aerospace Center (DLR) is chosen for the validation of our numerical models. The agreement between the model and the experiment would then provide evidence for a correct prediction of the ignition statistics in the transient jet.

In their experiment, a high-velocity cold methane jet ($U_i = 177$ m/s) emanated into a laminar co-flow of hot exhaust products of a lean hydrogen/air mixture ($U_o = 4$ m/s) at ambient pressure. The injector tube has a diameter of $D = 1.5$ mm, leading to a jet-Reynolds number of 16,000. Further information is given in Table 1. The co-flow mixture is obtained from the products of a lean-hydrogen flame ($\phi = 0.465$) that is fed to the system from a sinter-matrix. In Table 1, the remaining mass-fraction of the co-flow is included as additional nitrogen-content.

There are two versions of the same experiment – a (statistically) steady reference case and the pulsed case. In the latter, four phases are repeated; i. opening the valve and ramping up of the injection rate; ii. steady injection of the fuel at a constant mass flow rate; iii. ramping-down of the fuel's velocity, and closing of the valve; and iv. preparation for the next cycle.

Papageorge et al. [7, 8, 9, 10, 11] measured the composition and temperature fields for each pulse cycle using high-speed Rayleigh scattering. They presented a statistical database for the AI delay times and ignition kernels for the pulse cycles from 300 realizations. Fioltakis et al. [20] computed the (statistically) steady reference case using Reynolds Averaged Simulations with transported PDF for the chemistry.

3. Modeling Approach

3.1. Multi-dimensional FGM

Combustion was modeled with the Flamelet Generated Manifolds (FGM) technique [15] adapted for AI studies. An auto-igniting unsteady one-dimensional counter-flow flame (flamelet) was precomputed considering methane on the fuel side and hot and vitiated oxidizer on the other side with the GRI-3.0 mechanism [21] using FlameMaster by Pitsch [22]. This solver computes the flamelets in the mixture fraction space, where the spatial profile of the mixture fraction is presumed by an error function. The Lewis number was assumed to be unity. The ignition history extracted from this simulation was used to fill the manifold's first two dimensions, the mixture fraction Z as defined by Bilger et al. [23] and the progress

variable Y_p. The progress variable Y_p is defined as the sum of two major Y_{CO_2}, Y_{CO} and one ignition related species Y_{HO_2} [24]. The progress variable is normalized as in Eq. (1) for an easier table-access during the LES.

$$C = \frac{Y_p(Z) - [Y_p(Z)]_{min}}{[Y_p(Z)]_{max} - [Y_p(Z)]_{min}} \tag{1}$$

Eight unsteady flamelet calculations with different stoichiometric Scalar Dissipation Rates $\chi(Z_{st})$ (SDR) from 0.1 to 1000 1/s were included in the manifold's third dimension to account for the local effect of SDR on AI. The presumed error function of the mixture fraction in the one-dimensional solver is such adjusted that the SDR on the stoichiometry corresponds to these values. The included SDRs in the manifold are given in Fig. 1a, as marked on the distinctive S-shaped curve derived from 65 steady one-dimensional counter-flow simulations. Figure 1a shows that the steady and the unsteady flamelet simulations are in good agreement, which is a good indication that the unsteady simulations achieve sufficiently long simulation times.

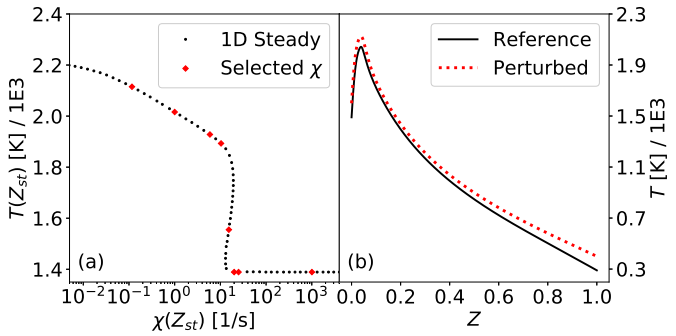

Figure 1: Left (a) shows the computed stoichiometric temperature from 65 different counter-flow steady flamelet simulations with varying SDR that are marked with black dots, and eight completely ignited unsteady flamelet simulations included in the look-up table that are marked by diamonds. The fully ignited unsteady flamelets that represent the reference (black) and the presumed perturbed states (red) used in the pressure dependency are visualized with the temperature profile in right (b).

3.2. Pressure dependency

To couple the tabulated chemistry to the density-based solver, the pressure dependency is included in the FGM by an efficient model by Saghafian et al. [19], which will be abbreviated as Compressible Flamelet Generated Manifolds (CFGM). (It should be noted that the pressure dependency is only included in the density-based solver, but not in the incompressible or low-Mach solver.)

In this model, the compressibility effects are represented as perturbations around the thermochemical state of the low-Mach number flamelet solutions, denoted as the reference state. The idea is to reconstruct the reaction rate source term $\dot{\omega}$ of the progress variable, the temperature T, the viscosity μ, the ratio of

Table 2: Fit parameters observed during the density-based LES.

Parameter	min.	max.	average
a_γ	$-2.3 \cdot 10^{-4}$	$4.2 \cdot 10^{-5}$	$-5.0 \cdot 10^{-6}$
a_μ	0	0.68	0.15
a_λ	0	2.89	0.47
a_ρ	-17.39	8.23	1.52

specific heats γ and the thermal conductivity λ of these perturbations by analytical functions.

$$\begin{aligned}\phi(\tilde{Z}, \widetilde{Z''^2}, \tilde{Y}_p, \widetilde{Y_p''^2}, \tilde{\chi}, \tilde{p}, \tilde{e}) = \\ \phi_0(\tilde{Z}, \widetilde{Z''^2}, \tilde{Y}_p, \widetilde{Y_p''^2}, \tilde{\chi}; \tilde{p}_0, \tilde{e}_0) + \\ \phi^*(\tilde{p}, \tilde{e}; \tilde{Z}, \widetilde{Z''^2}, \tilde{Y}_p, \widetilde{Y_p''^2}, \tilde{\chi})\end{aligned} \tag{2}$$

In this approach, a quantity ϕ is determined from the manifold as in Eq. (2), where p is the perturbed pressure and e is the internal energy including the chemical energy without the kinetic part. The corrected ϕ is evaluated from the ϕ_0 value at the reference state of pressure p_0 and internal energy e_0 and analytically interpolated towards the perturbed state that differs by ϕ^*.

$$\tilde{\gamma} = \tilde{\gamma}_0 + a_\gamma(\tilde{T} - T_0) \tag{3}$$

$$\tilde{\mu} = \tilde{\mu}_0 \left(\frac{\tilde{T}}{T_0} \right)^{a_\mu} \tag{4}$$

$$\tilde{\lambda} = \tilde{\lambda}_0 \left(\frac{\tilde{T}}{T_0} \right)^{a_\lambda} \tag{5}$$

$$\overline{\dot{\omega}} = \overline{\dot{\omega}}_0 \left(\frac{\overline{\rho}}{\overline{\rho}_0} \right)^{a_\rho} e^{-T_a(1/\tilde{T} - 1/T_0)} \tag{6}$$

Density is denoted as ρ, the temperature at the reference level is T_0 and a constant activation temperature T_a of 5000 is selected. The value of the activation temperature does not influence the simulations with mild-pressure perturbations, if only the value is greater than unity and is used to pre-compute the a_ρ from the reference and perturbed states and compute Eq. (6) during the LES - in other words, if the same T_a is used for table generation and table access.

The coefficients a_γ, a_μ, a_λ and a_ρ in Eqs. (3-6) are pre-computed from a presumed perturbed state during the flamelet calculations, and are mapped to the reference manifold to keep the manifold's dimensions the same. The presumed perturbed state was created by imposing a higher fuel temperature (400 K instead of 290 K) and oxidizer temperature (1600 K instead of 1490 K) at the boundaries of the unsteady flamelet

simulations. This presumed perturbed state with boundary temperature variations provides the basis to create all possible intermediate states that are accessed via the aforementioned non-linear interpolation. Alternatively, the background pressure variations can be considered that lead to the same intermediate states, hence the same conclusion. (A more extensive discussion is given in the original presentation of the model [19]). The temperature profiles of fully ignited unsteady flamelets that represent the reference and presumed perturbed states are shown in Fig. 1b.

$$\tilde{T} = T_0 + \frac{\tilde{\gamma}_0 - 1}{a_\gamma}\left(e^{a_\gamma(\tilde{e}-\tilde{e}_0)/\tilde{R}} - 1\right) \tag{7}$$

The values γ, μ, λ, $\dot{\omega}$, T are recomputed during the LES following Eqs. (3-7). The species' mass fractions are considered as frozen at the reference level, where this assumption linearises the equation of state due to the neglected species' mass fraction fluctuations. As the equation of state couples density and pressure, slightly limited degrees of freedom to represent compressibility effects are expected. However, a recent study suggests that this introduced linearisation error should be minimal for the flows that contain extensive nitrogen and mild pressure perturbations [25], similar to the presented case.

The results are initially stored in a three-dimensional equidistant look-up table, which is then accessed in the subsequent LES calculations by the transported mixture fraction $\tilde{Z}$, non-normalised progress variable $\tilde{Y}_p$, total energy E and analytically computed SDR $\tilde{\chi}$. The fit coefficients are given in Table 2.

It should be noted that the subgrid distribution of SDR is implicitly determined during the flamelet calculations from the mixture fraction's presumed error function.

3.3. Numerical setup

Our simulations were performed with the in-house LES and DNS solver PsiPhi [14, 26, 27] that is available in both density- and pressure-based formulations. Favre-filtered governing equations for mass, momentum, mixture fraction and progress variable were solved with a low-storage explicit Runge-Kutta scheme. The total energy including the chemical part is additionally transported during the density-based LES.

The convective fluxes of scalars were interpolated using a total variation diminishing (TVD) scheme with the CHARM limiter [28]. For the density-based solver, the convective fluxes of momentum were handled with a central differencing scheme blending over into a TVD scheme (MUSCL [29]) for Mach numbers above 0.2. For the pressure-based solver, a central differencing scheme for the convective fluxes of momentum was employed.

The inlet and the outlet boundaries of the density-based solver were prescribed by non-reflective Navier Stokes Characteristic Boundary Conditions (NSCBC) [30]. For both solvers, walls defined by immersed boundaries surrounded the geometry. A Power-law velocity profile was imposed at the inlet. The inflow turbulence was generated by the method developed by Klein et al. [31] in an efficient implementation by

Kempf et al. [32]. The integral length scale l_t and the turbulence intensity I_t were chosen as $0.205D$ and 5%, respectively.

The unresolved fluxes in momentum and scalars were estimated from eddy-viscosity and eddy-diffusivity approaches at a Turbulent Schmidt number Sc_t of 0.7. Turbulent viscosity ν_t was determined by Nicoud's σ-model [33]. The subgrid contributions of the Favre-filtered $\tilde{Z}$ and $\tilde{Y_p}$ were estimated via the top-hat filtered density function (FDF) method [34], as suggested by Floyd et al. [35], and extensively described by Rittler et al. [36].

$$\tilde{\chi} = 2(D + D_t)\nabla\tilde{Z}\nabla\tilde{Z} \tag{8}$$

An analytical expression was used to estimate the SDR, as given in Eq. (8). The sub-grid part of $\tilde{\chi}$ was modeled with a simplified version of the method by Girimaji and Zhou [37] by adding turbulent diffusivity $D_t = \nu_t/Sc_t$ to the molecular diffusivity D.

A linear function was used for both ramping up and down of the fuel mass flow over 0.5 ms. A total of 20 pulse cycles were phase-averaged to obtain converged statistics, requiring to simulate a real-time of one second. The waiting time between the pulses was 40 ms, corresponding to three co-flow advection times, and no interference was observed between the cycles. The first cycle was discarded from the statistics.

The simulations were performed in a domain 65x35x35 mm^3 on an equidistant Cartesian grid with $\Delta = 0.1$ mm spacing and 80 million cells throughout the computational domain at a temporal resolution of 0.7 μs (CFL criterion of 0.7). The computational domain includes the final 3 mm of the fuel injector tube. The simulation required 8.0E4 CPUh per pulse cycle, or a total of over 16.0E5 CPUh, using 3168 cores in parallel through MPI.

4. Results and discussion

4.1. Homogeneous Reactor

The AI delay time τ_{AI} depends on the local composition and temperature of the fuel/oxidizer mixture, as long as the local scalar gradients are low. An a-priori study of this case's ignition properties is presented first, based on several zero-dimensional homogeneous reactor simulations with the GRI-3.0 mechanism [21] using Cantera [38].

Figure 2a shows the mixing-line of the cold methane and the hot and vitiated oxidizer mixture (using the temperature values from the experiments) over mixture fraction. Figure 2b shows the temperature over AI delay time of six reactor simulations, where the initial composition and temperature values were taken from the mixing-line in Fig. 2a.

According to the reactor simulations, the leaner compositions with higher initial temperatures yielded a quicker ignition. The ignition occurred even for very lean mixtures, down to a mixture fraction value

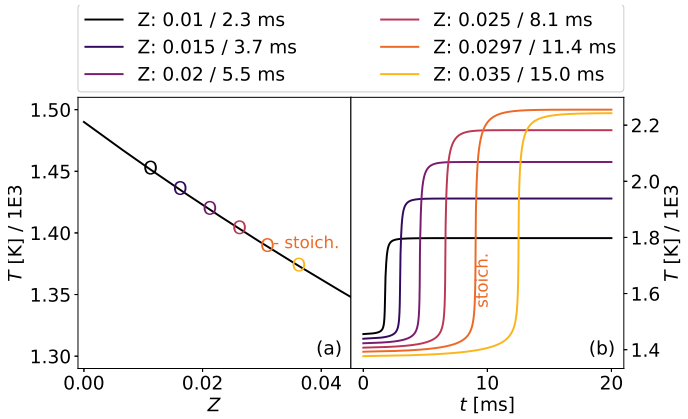

Figure 2: The mixing-line of the experimental composition over mixture fraction (a) and the reactor simulated temperature over time for different mixtures taken from the mixing-line (b) are presented.

of 0.0024 since the oxidizer temperature was higher than the activation temperature. The temperature in the reactor for extremely lean conditions (mixture fraction lower than 0.0024) did not exceed the ignition temperature threshold of 5% increase over the co-flow temperature. It was observed that the (colder) stoichiometric and rich mixtures ignited considerably later than the lean ones.

The AI delay times at the stoichiometric mixture fraction with different initial temperatures during the reactor computations are presented in Fig. 3a. The AI delay times were strongly reduced when the initial mixture temperature was increased. A temperature of 1284 K was required for the ignition to happen within a reasonable residence time.

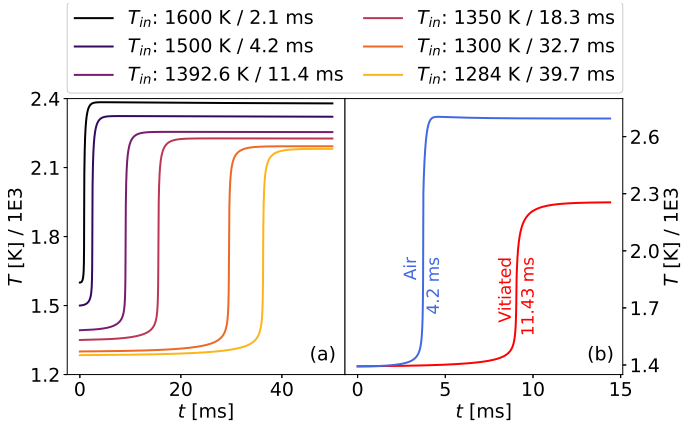

Figure 3: Simulated reactor temperature versus time (a) for stoichiometric mixture with different initial temperatures. 1392.65 K curve corresponds to the mixing line value and the 1284 K to the minimum required temperature for ignition to happen. The ignition in the vitiated co-flow and in the pure air (b) for stoichiometric mixture with the same initial temperature.

Figure 3b shows the reactor results of the temperature over time, where the ignition in the vitiated co-flow was compared to ignition in the air of the same temperature and mixture fraction. Vitiated oxidizer

led to a delayed ignition by 7 ms than the air. As expected, the temperature achieved in the hot air would be much higher, by 680 K.

AI in three-dimensional simulations should occur on the very lean side at the *most reactive* mixture fraction, with a value higher than 0.005. This *most reactive* mixture fraction could, however, shift to slightly richer zones due to turbulent interactions. The sensitivity of the initial temperature on the delay times could yield large deviations on the AI location, as an increase of the co-flow temperature from 1392.65 K to 1500 K leads to a 7.2 ms shorter ignition delay, whereas a decrease to 1300 leads to a 21.3 ms delay.

4.2. Steady jet flame

The simulations were validated with the experimental data ([20, 39]) during the (statistically) steady phase of the jet. A grid refinement study was carried out with the pressure-based LES for $\Delta = 0.25$ mm, 0.15 mm and 0.1 mm at 8, 26 and 80 million cells, respectively. A total of 150 instantaneous snapshots were averaged to obtain the mean data. The sample rate was 0.5 ms, which was much longer than the integral time scale $l_t/\tilde{U}'$ of 0.031 ms.

The mean methane mass fraction and temperature are presented along radial lines in Fig. 4, indicating that the coarse grid ($\Delta = 0.25$ mm) overpredicted the jet's penetration length at the centerline. It was observed that the results from medium and fine grids agree well to the experiments. The simulation with the fine grid ($\Delta = 0.1$ mm) was chosen for this study so that the scalar gradients at upstream locations were better described. The results converged well for the grids with medium and fine cell sizes, which yielded that the acquired statistics should be grid-independent.

Initially, it was not clear if the more cost-effective low-Mach number formulation would still be applicable for this particular free jet, which reaches a local Mach number of 0.7 in the center of the orifice. This high Mach number flow could be problematic to describe for a pressure-based solver. However, this jet is mainly decelerated by shear stresses and friction sources rather than by an adverse pressure gradient, and any sharp pressure rises during the initial pulse are avoided by ramping up the fuel mass-flow, so that pressure fluctuations are small. Therefore, the low-Mach formulation should still provide an acceptable description of the flow field. To test this hypothesis, the density-based solver with compressible FGM using four control parameters denoted as CFGM and the pressure-based solver with three control parameter denoted as FGM are compared against each other and the steady experiments, and later with the transient ones.

The radial profiles at four axial locations for mean and Root-Mean-Square (RMS) of methane mass fraction $\tilde{Y}_{CH_4}$ and temperature $\tilde{T}$ are given in Figs. 5 and 6. Upstream at 20 mm and 30 mm, both simulations predicted the jet-penetration length as in the experiments, as shown in Fig. 5. The mass fraction fluctuations upstream were predicted well, even though no a-priori information about the velocity fluctuations at the inlet was known. Further downstream at 40 mm and 50 mm, the simulations predicted a slightly wider jet. The rate of macro-mixing was underpredicted with CFGM, which yielded overestimated

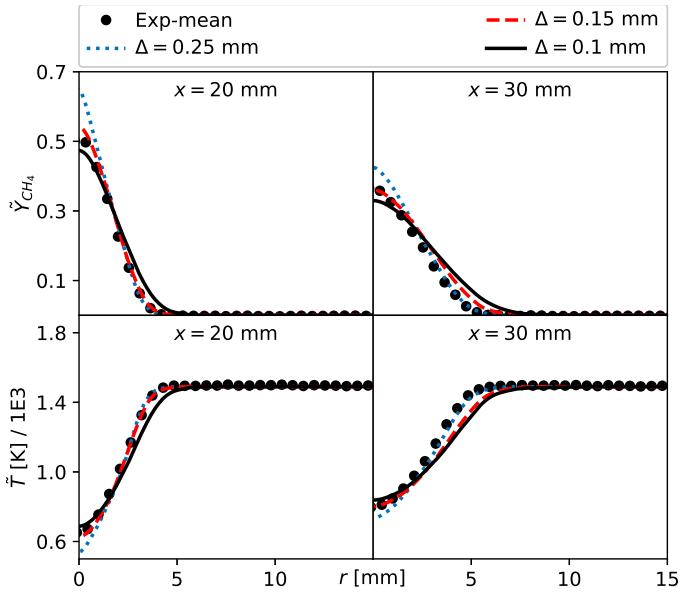

Figure 4: Mean methane mass fraction $\tilde{Y}_{CH_4}$ and temperature $\tilde{T}$ radial lines obtained from different grids using cell sizes of $\Delta = 0.25$ mm, 0.15 mm and 0.1 mm at 8, 26 and 80 million cells, respectively.

mass fractions at 50 mm. On the other hand, the fluctuations were in good agreement for both simulations.

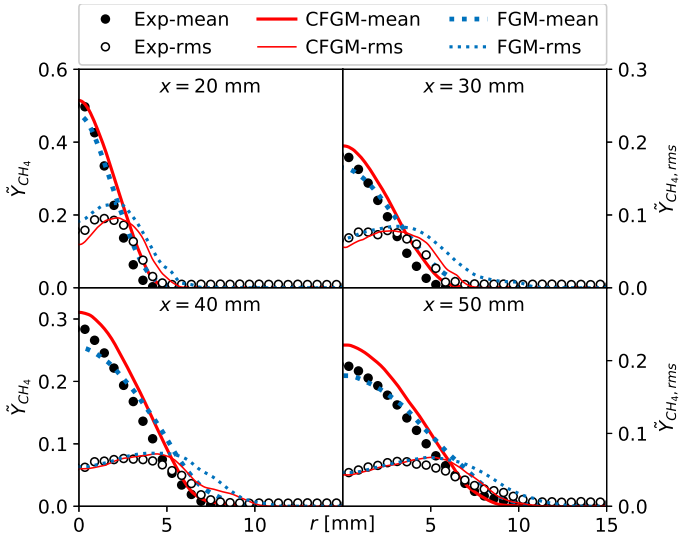

Figure 5: Radial profiles of mean and RMS of Mean methane mass fraction $\tilde{Y}_{CH_4}$ at four axial locations on the middle plane.

Figure 6 shows that downstream of 40 mm, the LES overpredicted the mean temperatures on the co-flow side for both CFGM and FGM approaches, as a result of the flame stabilizing a little too close to the burner. The emerged ignition spots caused a large-fluctuation of temperature values so that the RMS of temperature were also overpredicted.

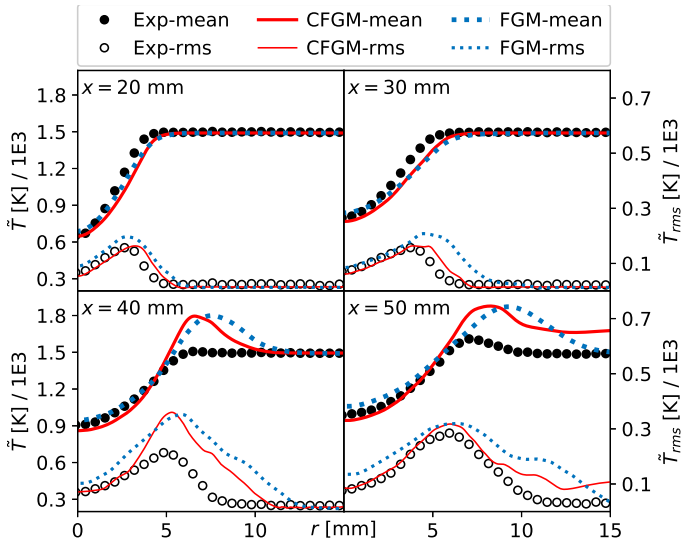

Figure 6: Radial profiles of mean and RMS of temperature $\tilde{T}$ at four axial locations on the middle plane.

Axial profiles of $\tilde{Y}_{CH_4}$ and $\tilde{T}$ for the simulations and the experiment are presented in Fig. 7. The mixing decay of the jet along the centerline was well predicted by both methods, where CFGM yielded better mass fractions upstream, and FGM showed slightly better agreement downstream. A remarkable difference was that the jet penetration core from CFGM was slightly shorter than the FGM. For the simulated temperature, slightly lower values do result from the compressible simulation, which is in line with more unburned methane predicted by this simulation. Overall, however, compressible and incompressible simulations agree sufficiently well with the experiments to enable cost-effective incompressible simulations (FGM) of the pulsed flame.

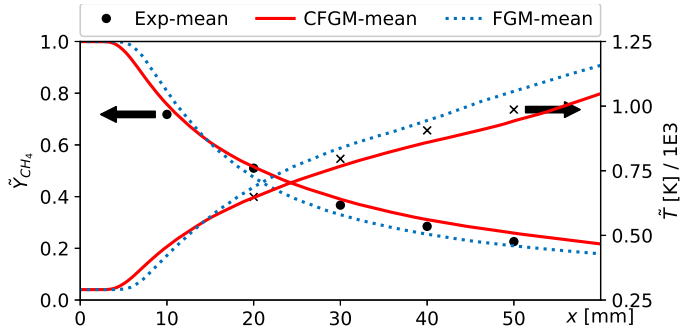

Figure 7: Axial profiles of mean Mean methane mass fraction $\tilde{Y}_{CH_4}$ (circles) and temperature $\tilde{T}$ (crosses) on the centerline.

4.3. Pulsed jet flame

The density-based solver was estimated to be almost one order of magnitude more costly than the pressure-based variant due to the smaller time-step and more expensive access to a higher-dimensional chemistry table. This difference in cost forced us to perform the 20 cycles with the pressure-based solver.

Two pulses were simulated with the density-based solver for comparison at the cost of 20 incompressible cycles (initial cycle was discarded from the statistics).

This part uses the experimental data available from DLR [7, 8, 9, 10, 11]. The temporal evolution of the jet during a cycle is illustrated in Fig. 8. The pinched vortex ring appeared after the injection quickly disintegrated to the hot co-flow. As the jet penetrated the domain, the mixing layer thickness became potentially larger. The potential core, however, remained as short as 8 mm. For more physical insight into the behavior of a pulsed jet (non-reactive), the reader is kindly referred to one of our previous papers [14].

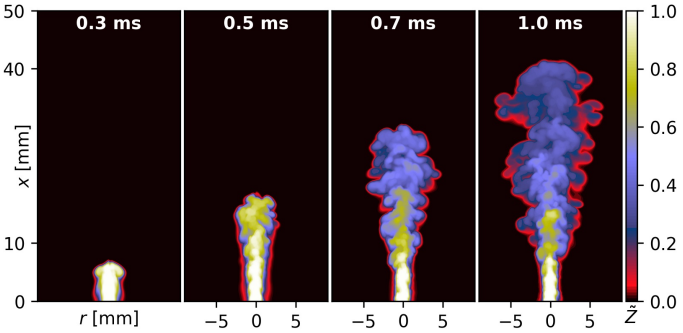

Figure 8: Temporal evolution of the jet with snapshots of mixture fraction $\tilde{Z}$ from the second pulse cycle.

The formation of an AI kernel over time is illustrated in Fig. 9 by snapshots of temperature for the second pulse, where AI happened at 2.52 ms. The horizontal cross-section in Fig. 9 is moved with the flow to track the AI kernel. A red iso-line corresponding to a five percent temperature increase from $T_o = 1490$ [K] is defined as the outer limit of the AI kernel, the black iso-lines mark the stoichiometric mixture fraction.

Figure 9 shows a spot with a local temperature slightly higher than the co-flow temperature T_o at 2.57 ms. This AI kernel candidate at $(x, y, z) = [36.3, 0.3, 7.8]$ mm was on the lean side of the jet's mixing layer, this then rapidly grew and ignited the flame. The AI kernel remained on the lean-side during its expansion, where a small part of this kernel aligned with the stoichiometric mixing layer later on. At later times, several AI kernels started forming at downstream locations as well. As expected, the ignition spots appeared on pseudo-random locations, correlated to the mixing and other parameters, such as local SDR [1].

Evidence was also found that the flame ignited not at stoichiometry but at the most-reactive mixture fraction Z_{MR} [1]: During the second pulse cycle, AI was first observed at $Z_{MR} = 0.01$, as in Fig. 9. The leanest AI event was observed in the fourteenth cycle on a mixture fraction of 0.008. On the contrary, the richest AI happened in the eighteenth cycle on a mixture fraction of 0.018. Through 20 pulses, the average Z_{MR} was estimated as 0.013, which was in a good agreement with the reactor simulation result. The variations of Z_{MR} between the cycles exceeded 30%, and is likely a result of turbulence and its effect on mixing and residence times.

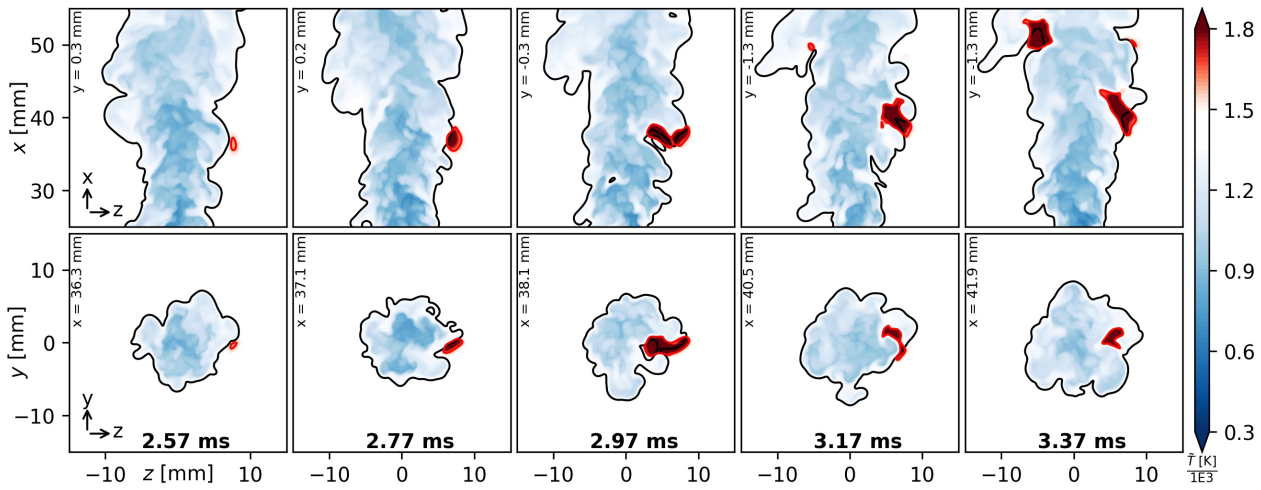

Figure 9: Snapshots of temperature $\tilde{T}$ field of an ignition event during the second pulse cycle. The contour-planes are sliced on the position where the AI is occurring. Two view-perspectives of the jet, side view (top row) and top view (bottom row) are given for precise AI location. The black iso-line indicates the stoichiometric mixture fraction $\tilde{Z}_{st}$, and the red iso-line represents five percent increase from T_o. (For better interpretation, please refer to the web version.)

4.4. Cycle variations

To identify the cycle variations, the cycle- and volume - averaged (over the entire domain) temperature and the absolute value of the heat release rate over the cycle time are presented in Figs. 10a-b. During the acceleration phase, Figure 10a shows initially decreasing averaged temperatures due to the freshly injected cold fuel, rapidly cooling the system, followed by an increase due to ignition. Meanwhile in Fig. 10b, a monotonic increase of averaged absolute heat release rate can be seen until the flame stabilizes. It was found that the temperature increased marginally after the flame stabilized. During the deceleration phase, the system cooled down to T_o in less than 20 ms.

Prior to the ignition, all cycles behaved similarly. The dispersion of the AI delay times made the cycles show slightly different temperature curves. Interestingly, the highest achieved averaged temperatures varied between cycles. This was due to the position of the ignition, where the flame that appeared closer to the burner increased the average temperatures. This wide dispersion in the temperature curves was not observed in the averaged absolute heat release rate.

An important observation was made during the deceleration phase, where the absolute heat release rate further increased to a maximum value. Meanwhile, the averaged temperature of the system dropped initially just after the closing of the inlet valve, then a slight temperature rise was observed again. During this phase, the heat release showed great variations between cycles. A possible explanation is that the flame re-ignited close to the trailing edge of the jet at the locations where SDR was decreasing. This finding may be particularly important for combustors with fuel injection and might explain some types of cyclic variation observed in internal combustion engines, which is a topic suggested for further investigation.

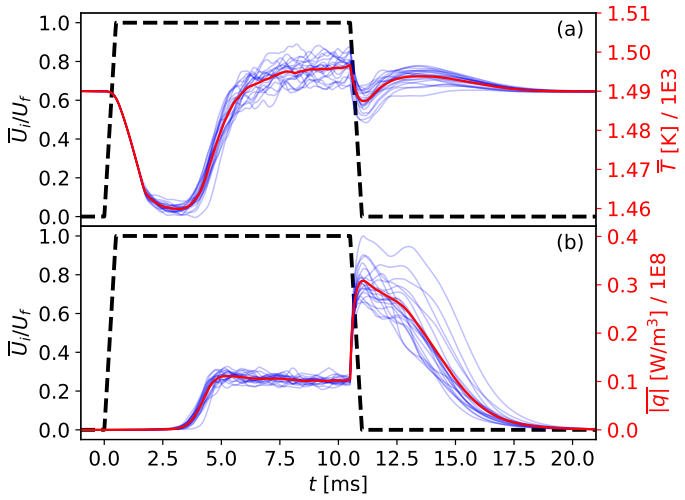

Figure 10: Cycle- and volume-averaged temperature $\tilde{T}$ (a) and absolute value of the heat release rate $|\tilde{q}|$ (b), together with the velocity pulses (dashed). The transparent blue lines represent different cycles.

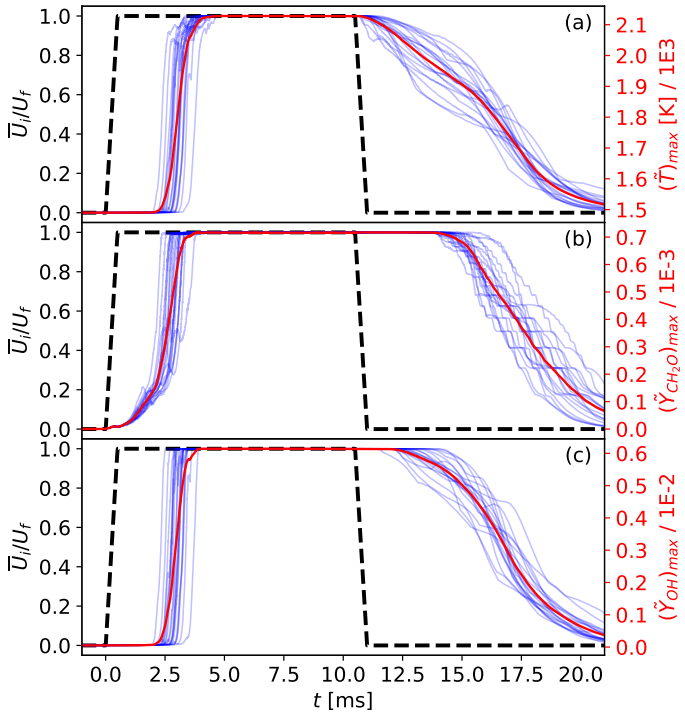

Figure 11: Cycle-averaged maximum temperature $\tilde{T}$ (a), mass fractions of formaldehyde $\tilde{Y}_{CH_2O}$ (b) and hydroxyl $\tilde{Y}_{OH}$ (c), together with the velocity pulses (dashed). The transparent blue lines represent different cycles.

The investigation of the cycle variations continues with the cycle-averaged maxima of temperature, mass fractions of formaldehyde Y_{CH_2O} and hydroxyl Y_{OH} over the duration of a cycle, which are presented in Figs. 11a-c. The wide AI delay time distribution is noticeable in the temperature curves in Fig. 11a. In

some cycles, the maximum temperature dropped down due to the *failed* ignition in premature AI spots. This behavior was typical since the turbulent flow structures often destroyed AI kernels. Similar behavior was observed for the hydroxyl, however unlike the temperature, hydroxyl was more monotonically increasing (Fig. 11c). The ignition related species formaldehyde started with a small increase at early times, then built up in the system at an increasing rate (Fig. 11b), slightly quicker than for the temperature and the hydroxyl species. The maximum value of the formaldehyde mass fraction was seen approximately at the same time when the temperature curve rose fastest (maximum gradient). The maximum value of the temperature and species' mass fractions in the system was constant due to the nature of the tabulated chemistry.

4.5. Auto-ignition

For the definition of the AI delay time, criteria used for zero- or one-dimensional cases cannot simply be applied. Instead, we used several known descriptions and extract the information from the LES. The spatial location of the highest temperature, formaldehyde and hydroxyl mass fractions were written out, as the data in the previous Figs. 11a-c. From this information, three AI delay times τ_{AI} were determined by the time when:

τ_{AI_1} – The temperature values exceeds a five percent increase over the co-flow temperature T_{co}.

τ_{AI_2} – The maximum accumulation of formaldehyde was reached.

τ_{AI_3} – The hydroxyl values exceeds a five percent increase over the co-flow values.

The definition of τ_{AI_1} corresponds to the method used in the experiments [10].

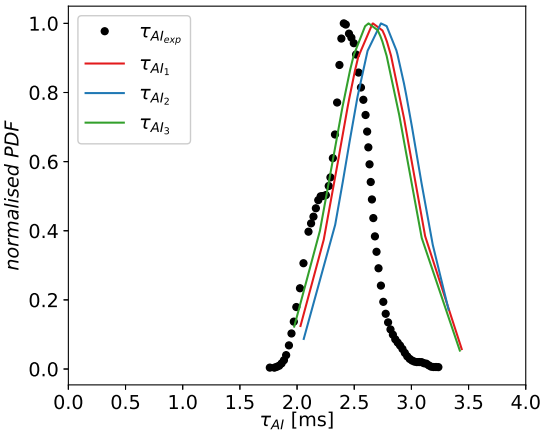

Figure 12: Normalized PDFs of AI delay times from the simulations and the experiments. The criteria for AI leading to $\tau_{AI_{1-3}}$ are given in the text.

The numerically estimated delay times are compared to the experimental ones by their Probability Density Functions (PDF) in Fig. 12, where the delay times in 20 cycles were binned into 0.2 ms intervals

to achieve the PDF curve. The experiments used 300 samples to generate the experimental PDF. It can be seen from Fig. 12 that any of these different AI definitions would yield a similar outcome.

By using the τ_{AI_1} in the LES, the quickest and the slowest ignition happened at 2.16 ms (eighth cycle) and 3.57 ms (third cycle), respectively. The computed mean delay time was 2.64 ms, which was 0.13 ms longer than the experimental one. It was seen that using delay time estimations conditioned on the hydroxyl species yielded a 0.04 ms shorter delay time, whereas formaldehyde yielded a 0.06 ms longer delay time than the temperature based criterion.

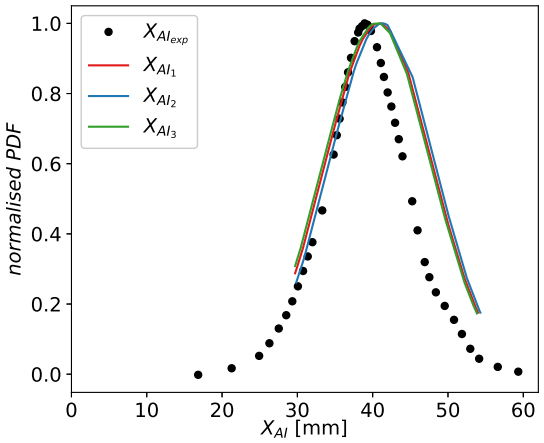

Figure 13: Normalized PDFs of AI height above the burner from the simulations and the experiments. The criteria for AI are the same as in Fig. 12 and as given in the text.

The PDF of the locations of the ignition spots are shown in Fig. 13. The AI height was defined as the axial distance of the initial ignition spot from the burner exit. The AI heights with both temperature, formaldehyde and hydroxyl based definitions provided almost identical results, as expected. The estimated heights were in good agreement with the experiments, where the deviation of average computed height to the experimentally determined one was just under 2 mm. The experiments showed a slightly narrower distribution, as presented in Fig. 13.

The agreement of ignition heights between the computed and experimental ones raised a question about the underpredicted flame lift-off height during the steady runs (Fig. 6). It was evident that the flame should stabilize slightly further downstream from the initial AI spot, whereas this was not observed during the simulations. At this point, it is hard to conclude on the cause of this deviation. It should however be noted that the flamelets were created to model auto-ignition rather than edge-flame propagation, so that flame propagation may be a major contributor to the deviation observed.

The spatial locations of the AI spots for the 20 pulses are visualized in Fig. 14. The AI spots are defined from τ_{AI_1}. Figure 14 shows that there is no pattern between the cycle number and the AI location. The nearest AI spot was during the seventh cycle at an axial distance of 29.7 mm, whereas the farthest one

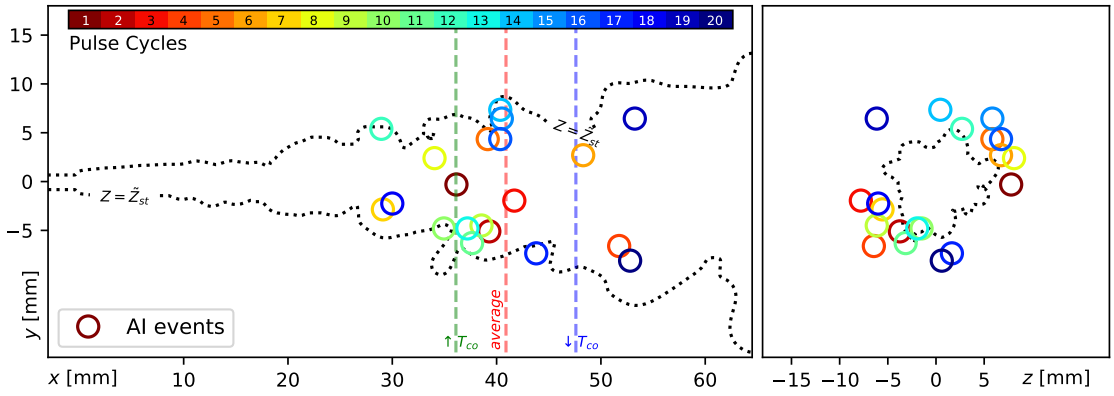

Figure 14: The spatial location of the AI spots for 20 pulses, side view (left) and top view (right). Colors represent individual cycle and the black iso-line *qualitatively* indicates the stoichiometric mixture fraction $\tilde{Z}_{st}$. Blue and green lines are AI height shifts with respect to the average height (red line) from a 10 K increase and decrease of the co-flow temperature, respectively. (For better interpretation of the contours, please refer to the web version.)

happened during the 19^{th} cycle with 54 mm. This Figure 14 also shows that the AI spots for different cycles always emerge on the lean side of the flame, however, in a completely random manner.

The AI locations were found to be very sensitive to the local temperature and hence the temperature of the vitiated co-flow. Similar observations have been made during the AI studies in Diesel engine relevant conditions of n-Heptane spray flames [40], and also in the experiments of this case [8]. A slight variation of the local temperature would shift the location of the AI spots. To estimate the sensitivity of the AI location on the co-flow temperature, we have conducted auto-ignition studies in a homogeneous reactor for a 10 K increased and 10 K decreased co-flow temperature, leading to 0.2 ms earlier and 0.28 ms later ignition. For a mean velocity of 24 m/s at the point of ignition, this would translate to a $\pm$ 5.5 mm shift. This means that the point of ignition would move 14 % towards or away from the burner if the co-flow temperature is altered by only 10 K, as qualitatively represented in Fig. 14 by dashed lines.

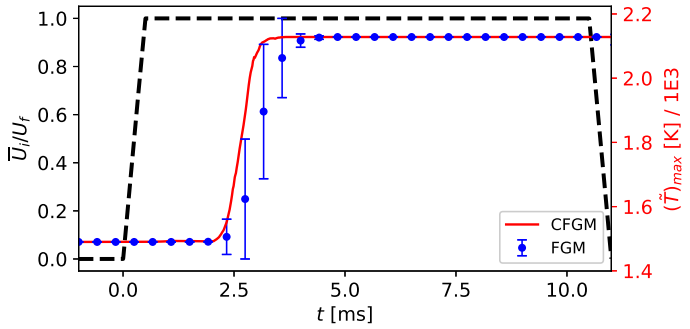

Figure 15: Comparison of cycle-averaged maximum temperature $\tilde{T}$ with compressible solver (CFGM) to the incompressible one (FGM), together with the velocity pulses (dashed). The blue error bars represent standard deviation between cycles to the cycle-averaged one.

To test again if a compressible simulation would show different results than an incompressible one, we have simulated one pulse with the compressible code (at the cost of ten cycles with the incompressible code). Ignition in the compressible simulation agrees with ignition in the incompressible cycles, as illustrated in Fig. 15 that shows how the compressible cycle is located within one standard deviation of the incompressible cycles.

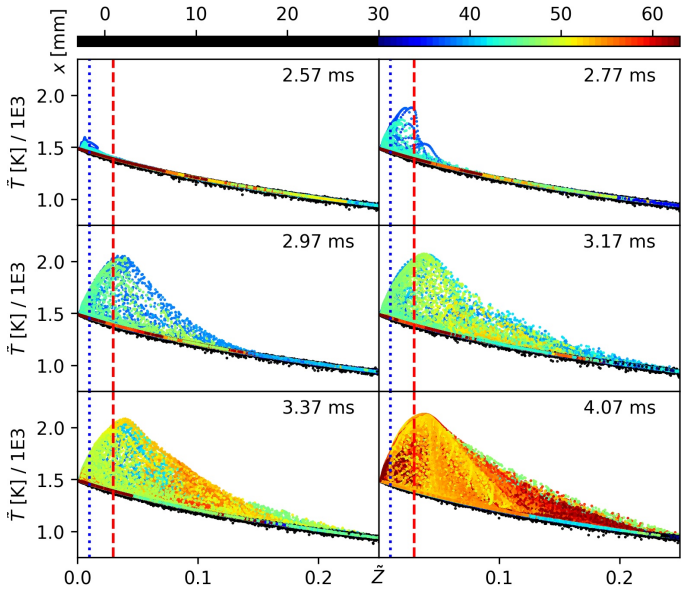

Figure 16: The temperature $\tilde{T}$ over the mixture fraction $\tilde{Z}$, colored by the distance from the burner during the ignition event of second pulse. The blue and the red lines denote most reactive Z_{MR} and stoichiometric Z_{st} mixture fractions, respectively.

Finally, Fig. 16 shows the scatter plots of the temperature over the mixture fraction at several times of the pulse, colored by the distance from the burner. Several candidate AI kernels emerged on the very lean side at 2.57 ms close to the inlet. During the ignition, the AI kernel expanded from Z_{MR} at the axial distance of 36 mm. This was followed by the increase of the temperature on the rich zones at a further downstream location of 45 mm. After the ignition, the axial distance of high temperatures was mostly shifted towards the rich zones at most downstream locations.

5. Conclusions

The pulsed auto-igniting (AI) jet flame in a vitiated co-flow experiment from DLR [7, 8, 9, 10, 11] was numerically investigated. The targets were to analyze the weak compressibility effects and the reproducibility of the auto-ignition properties that differ on each injection. In this configuration, the local Mach number was as high as 0.7 due to the injection velocity. Two LES strategies were tested and compared: A pressure-based solver with a tabulated chemistry that used mixture fraction, progress variable and mixture fraction's dissipation rate as the control parameters and a density-based solver that used the same chemistry model, but

with added pressure as the control parameter to couple the constant pressure flamelets with the pressure perturbations. With both approaches, a satisfactory agreement was obtained between the LES and the experiments for the (statistically) steady jet.

The predicted mixing dynamics were satisfactory, however, the flame lift-off heights were slightly under-predicted, which made the qualitative comparisons of the computed and measured temperature lines where the flame stabilized more difficult. The density-based model showed slightly warmer zones close to the burner. Interestingly, the temperature rise on the centerline in the density-based solver was slower than the pressure-based one.

The pressure-based solver was run over 20 pulses, where a single injection was carried out using the density-based solver. An important observation was also that the highest heat release did not occur during the injection phase of the jet but during the deceleration. An explanation could be that new AI spots emerge on the relaxed flow-field near the inlet, re-igniting the flame. The *most reactive* mixture fraction determined from the zero-dimensional reactor calculations were similar in the three-dimensional cases. Due to the turbulent interactions, the variation of this special composition was found between 0.008 and 0.18, which means that the AI always happened in the lean mixtures as evident in the literature [1].

The computed transient jet captured the AI dynamics well. The estimated AI delay times and heights were in the experimental range. The average ignition occurred slightly later and farther away than in the experiments. The shortest and the longest AI heights deviated more than 25 mm between these pulses. On the other hand, the jet ignited at a time between 2 and 3.5 ms. The AI dynamics estimated with a density-based solver did not deviate from the ones estimated with the pressure-based solver.

A strong sensitivity of the local temperature to the AI dynamics was observed, where a slight temperature variation of 20 K in the co-flow resulted in a 0.46 ms and 11.5 mm shift in the AI delay time and height, respectively. It was estimated that only a 4 K, or 0.3% decrease of the co-flow temperature would yield our AI statistics to perfectly match the experimentally obtained ones - a rather satisfactory agreement, considering the uncertainties involved.

Acknowledgments

The authors gratefully acknowledge the financial support by the state North-Rhine-Westphalia, Germany, and the computing time granted on magnitUDE (DFG grant INST 20876/209-1 FUGG).

References

[1] E. Mastorakos, Ignition of turbulent non-premixed flames, Prog. in En. Comb. Sci. 35 (1) (2009) 57–97.

[2] L. J. Spadaccini, M. B. Colket, Ignition delay characteristics of methane fuels, Prog. in En. Comb. Sci. 20 (5) (1994) 431–460.

[3] G. Cho, D. Jeong, G. Moon, C. Bae, Controlled auto-ignition characteristics of methane–air mixture in a rapid intake compression and expansion machine, Energy 35 (10) (2010) 4184–4191.

[4] C. N. Markides, E. Mastorakos, An experimental study of hydrogen autoignition in a turbulent co-flow of heated air, Proc. Combust. Inst. 30 (1) (2005) 883–891.

[5] E. Mastorakos, T. A. Baritaud, T. J. Poinsot, Numerical simulations of autoignition in turbulent mixing flows, Combust. Flame 109 (1) (1997) 198–223.

[6] P. Domingo, L. Vervisch, D. Veynante, Large-eddy simulation of a lifted methane jet flame in a vitiated coflow, Combust. Flame 152 (3) (2008) 415–432.

[7] C. M. Arndt, J. D. Gounder, W. Meier, M. Aigner, High-speed imaging of auto-ignition of pulsed methane jets in a hot vitiated co-flow, App. Phy. B 108 (2) (2012) 407–417.

[8] C. M. Arndt, R. Schießl, J. D. Gounder, W. Meier, M. Aigner, Flame stabilization and auto-ignition of pulsed methane jets in a hot coflow: Influence of temperature, Proc. Combust. Inst. 34 (1) (2013) 1483–1490.

[9] M. J. Papageorge, C. M. Arndt, F. Fuest, W. Meier, J. A. Sutton, High–speed mixture fraction and temperature imaging of pulsed, turbulent fuel jets auto-igniting in high-temperature, vitiated co-flows, Exp. Fluids 55 (7) (2014) 1763–1783.

[10] C. M. Arndt, M. J. Papageorge, F. Fuest, J. A. Sutton, W. Meier, M. Aigner, The role of temperature, mixture fraction, and scalar dissipation rate on transient methane injection and auto-ignition in a jet in hot coflow burner, Combust. Flame 167 (2016) 60–71.

[11] M. J. Papageorge, C. M. Arndt, F. Fuest, W. Meier, J. A. Sutton, Erratum to: High–speed mixture fraction and temperature imaging of pulsed, turbulent fuel jets auto-igniting in high-temperature, vitiated co-flows, Exp. Fluids 57 (1) (2016) 14–20.

[12] T. Echekki, J. H. Chen, Direct numerical simulation of autoignition in non-homogeneous hydrogen-air mixtures, Combust. Flame 134 (3) (2003) 169–191.

[13] R. P. Lindstedt, E. M. Vaos, Transported pdf modeling of high-reynolds-number premixed turbulent flames, Combust. Flame 145 (3) (2006) 495–511.

[14] E. Inanc, M. T. Nguyen, S. Kaiser, A. M. Kempf, High-resolution LES of a starting jet, Comp. Fluids 140 (2016) 435–449.

[15] J. A. van Oijen, L. P. H. de Goey, Modelling of premixed laminar flames using flamelet-generated manifolds, Comb. Sci. Tech. 161 (1) (2000) 113–137.

[16] P. Nakod, R. Yadav, P. Rajeshirke, S. Orsino, A comparative computational fluid dynamics study on flamelet-generated manifold and steady laminar flamelet modeling for turbulent flames, J. Eng. Gas Turb. Power 136 (8) (2014) 081504.

[17] J. A. van Oijen, A. Donini, R. J. M. Bastiaans, J. H. M. ten Thije Boonkkamp, L. P. H. de Goey, State-of-the-art in premixed combustion modeling using flamelet generated manifolds, Prog. in En. Comb. Sci. 57 (2016) 30–74.

[18] Y. Moule, V. Sabelnikov, A. Mura, Highly resolved numerical simulation of combustion in supersonic hydrogenair coflowing jets, Combust. Flame 161 (10) (2014) 2647–2668.

[19] A. Saghafian, High-fidelity simulations and modeling of compressible reacting flows, Ph.D. thesis, Stanford University, California, USA (2014).

[20] A. Fiolitakis, P. Ess, P. Gerlinger, M. Aigner, Anwendung eines transportgleichungs-PDF-verfahrens zur berechnung der selbstzündung eines methan-freistrahles, Proc. 27. Deutscher Flammentag (2015) 617–628.

[21] G. P. Smith et al., Gri-mech 3.0, <http://combustion.berkeley.edu/gri-mech/> (2000).

[22] H. Pitsch, A C++ computer program for 0-D combustion and 1-D laminar flame calculations, RWTH Aachen (1998).

[23] R. W. Bilger, The structure of diffusion flames, Comb. Sci. Tech. 13 (1976) 155–170.

[24] C. Bekdemir, B. Somers, L. P. H. de Goey, DNS with detailed and tabulated chemistry of engine relevant igniting systems, Combust. Flame 161 (1) (2014) 210–221.

[25] G. Ribert, P. Domingo, L. Vervisch, Analysis of sub-grid scale modeling of the ideal-gas equation of state in hydrogen-

oxygen premixed flames, Proc. Combust. Inst.doi:10.1016/j.proci.2018.07.054.

[26] A. M. Kempf, B. J. Geurts, J. C. Oefelein, Error analysis of large-eddy simulation of the turbulent non-premixed sydney bluff-body flame, Combust. Flame 158 (12) (2011) 2408–2419.

[27] F. Proch, P. Domingo, L. Vervisch, A. M. Kempf, Flame resolved simulation of a turbulent premixed bluff-body burner experiment. part i: Analysis of the reaction zone dynamics with tabulated chemistry, Combust. Flame 180 (2017) 321–339.

[28] G. Zhou, Numerical simulations of physical discontinuities in single and multi-fluid flows for arbitrary mach numbers, Ph.D. thesis, Chalmers Uni. of Tech., Goteborg, Sweeden (1995).

[29] S. Camarri, M. V. Salvetti, B. Koobus, A. Dervieux, A low-diffusion muscl scheme for LES on unstructured grids, Comp. Fluids 33 (9) (2004) 1101–1129.

[30] T. Poinsot, D. Veynante, Theoretical and Numerical Combustion, RT Edwards, CNRS Toulouse, France, (2005), p. 472.

[31] M. Klein, A. Sadiki, J. Janicka, A digital filter based generation of inflow data for spatially developing direct numerical or large eddy simulations, J. Comp. Phy. 186 (2) (2003) 652–665.

[32] A. M. Kempf, M. Klein, J. Janicka, Efficient generation of initial-and inflow-conditions for transient turbulent flows in arbitrary geometries, Flow, Turb. Comb. 74 (1) (2005) 67–84.

[33] F. Nicoud, H. B. Toda, O. Cabrit, S. Bose, J. Lee, Using singular values to build a subgrid-scale model for large eddy simulations, Phy. Fluids 23 (8) (2011) 085106.

[34] J. P. Legier, T. J. Poinsot, D. Veynante, Dynamically thickened flame LES model for premixed and non-premixed turbulent combustion, Proc. Summer Prog. (2000) 157–168.

[35] J. Floyd, A. M. Kempf, A. Kronenburg, R. H. Ram, A simple model for the filtered density function for passive scalar combustion LES, Combust. Theory Mod. 13 (4) (2009) 559–588.

[36] A. Rittler, F. Proch, A. M. Kempf, LES of the Sydney piloted spray flame series with the PFGM/ATF approach and different sub-filter models, Combust. Flame 162 (4) (2015) 1575–1598.

[37] S. S. Girimaji, Y. Zhou, Analysis and modeling of subgrid scalar mixing using numerical data, Phy. Fluids 8 (1996) 1224–1236.

[38] D. G. Goodwin, Cantera, <code.google.com/p/cantera> (2009).

[39] C. M. Arndt, Personal communication (26.11.2016).

[40] Y. M. Wright, O. N. Margari, K. Boulouchos, G. De Paola, E. Mastorakos, Experiments and simulations of n-Heptane spray auto-ignition in a closed combustion chamber at diesel engine conditions, Flow, Turb. Comb. 84 (1) (2010) 49–78.